

Influence of the microstructure of TMT reinforcing bars on their corrosion behavior in concrete with chlorides

A. Bautista^{a1}, J.C. Pomares^b, M.N. González^c, F. Velasco^a

^a University Carlos III of Madrid. Material Science and Engineering Department-IAAB.
Avda. Universidad 30. 28911 Leganés, Madrid, Spain

^b University of Alicante. Civil Engineering Department. Carretera San Vicente del
Raspeig s/n, 03690 San Vicente del Raspeig, Alicante, Spain

^c Universidad Politécnica de Madrid. Escuela Técnica Superior de Edificación. Avda.
Juan de Herrera 6. 28040 Madrid, Spain

Abstract

Thermomechanically treated (TMT) carbon steel bars, often known as “TempCore” bars, are commonly used as reinforcements in concrete structures. TMT causes the formation of a martensite case in the outer surface of the bars, increasing their hardness, while the remaining ferritic-perlitic core maintains the typical ductility of hot rolled bars. In this work, the effect of this TMT induced microstructure on the development of pitting attacks in chloride media has been analyzed in depth. Electrochemical impedance spectroscopy (EIS) measurements and polarization curves have been carried out in simulated pore solutions to understand the effect of the presence of different phases in the microstructure and to quantify the strength of the galvanic couple that the outer martensite can form with the inner core. Moreover, accelerated corrosion tests in chloride contaminated concrete slabs have also been performed. Bars from six different slabs where corrosive attack has been forced for different times have been studied. The shape of the main pits in the bars corroded in concrete has been analyzed through optoelectronic microscopy and the results obtained prove that the depth of the attack is related to the microstructure of the TMT bars.

Keywords: corrosion; pitting; chloride; concrete; thermomechanical treatment; carbon steel; galvanic coupling.

¹ Corresponding author. E-mail address: mbautist@ing.uc3m.es

30 **1. Introduction**

31 Reinforcing steel bars are usually embedded in concrete to increase the tensile
32 properties of this material. Cold rolled carbon steel bars can offer higher mechanical
33 strengths than traditional hot rolled bars [1,2], but the former are less ductile than the
34 latter. Moreover, the stresses in the microstructure of cold rolled bars can make them
35 more prone to corrosion [3], and they present offer worse after-fire mechanical
36 properties [1,2]. To increase the mechanical properties of hot rolled carbon steel bars,
37 the addition of microalloying elements as well as thermomechanical treatment (TMT),
38 can be used [4]. The addition of carbon in amounts ranging between 0.3 and 0.5%
39 hardens the steel, but its bendability and weldability decrease [5].

40 TMT bars, often known as “TempCore” bars, are manufactured by passing the
41 red heated steel -just after the rolling process- through a chamber with a control water
42 flow that quenches the outer surface of the bars, while their core remains hot as
43 austenite [6]. A martensite case is formed in the outer part of the bar. Then, in the core,
44 the austenite is transformed into ferrite and perlite through a slow cooling, while the
45 heat dissipated from the center of the bar to the surface causes the self-tempering of
46 the previously formed martensite [7]. The martensitic case formed in the outer surface
47 of the bars increases their hardness [8], while the remaining ferritic-perlitic core
48 maintains the typical ductility of hot rolled bars. The final strength of the TMT rebars
49 depends on the thickness of the outer tempered martensitic case as well as on the
50 distribution of other phases inside the core of bar [9]. Nowadays, the use of TMT
51 carbon steel bars has become common for reinforcing of concrete structures in Europe.
52 The TMT bars reduce the amount of steel needed for reinforcing a given concrete
53 structure as well as the global economic cost of the structure.

54 There are studies published on the influence of the microstructure of TMT
55 carbon steel bars on the fracture mode and ultimate tensile strength of the bars [6].
56 Moreover, TMT bars have shown better results in tensile and impact tests than direct
57 air-cooled microalloyed hot rolled bars [10]. The influence of high-temperature
58 exposure on the mechanical properties of the TMT bar is a point that has also been
59 studied [1,11], with their results being worse than those shown for traditional hot-rolled
60 carbon steel bars [1]. The fatigue performance of TMT bars has also been investigated
61 [12].

62 The corrosion performance of the steel reinforcements is another key factor for
63 the in-service performance of the structures. The alkaline solution inside the concrete
64 pore should be able to guarantee the chemical durability of the steel. However, factors

65 such as the presence of chlorides [13] or the decrease of the pore solution pH caused
66 by carbonation [14] often provoke the active corrosion of the reinforcing steel bars.
67 Microalloying elements that are able to improve the corrosion resistance of the steel
68 bars can also be added to TMT bars [15].

69 There is a corrosion study carried out with TMT bars where weight losses after
70 sea water and fresh water immersions were measured [3]. The results obtained in this
71 research suggest that the corrosion resistance of TMT bars could be higher than that of
72 conventional hot rolled reinforcing bars. Another corrosion study with TMT bars also
73 reports weight losses in NaCl solutions [4]. Recent preliminary results on about the
74 effect of the galvanic connection between TMT and conventional reinforcement steels
75 on their corrosion performance in simulated pore solutions have also been published
76 [16].

77 Moreover, it has been conclusively proved that the morphology of the pits is a
78 key factor influencing the tensile [17-19] and the fatigue [20,21] behaviors of the
79 reinforcing bars, and so, it determines the likelihood of dangerous pathologies or in-
80 service failures for the structures. The relationship between the microstructure of the
81 reinforcing bars and their pit morphology has been analyzed in depth for stainless steel
82 corrugated bars in simulated pore solutions [22]. There are also previous studies about
83 corrosion development of carbon steel in concrete [23,24], but they have not
84 considered the possible influence of the specific microstructure that appears in the bars
85 after TMT.

86 The frequent use of TMT bars and the clear interest of corrosion performance
87 evidence the need for obtaining more complete information about how the phases
88 present in their microstructure can influence the development of the attack in the bars.
89 In this work, the influence of the microstructure originated by the TMT on the corrosion
90 behavior of reinforcing bars is analyzed in solution tests, using different electrochemical
91 techniques. The obtained results are verified through a morphological analysis of the
92 shape of the main pits detected in bars corroded in concrete slabs.

93 **2. Experimental**

94 Carbon steel TMT bars type B-500-SD (UNE 36065) with 12-mm of diameter
95 were used for this study. The chemical composition of the bars was determined from X-
96 ray fluorescence and combustion infrared detection of C and S, which can be seen in
97 **Table 1**. The alloying content of this bars, makes their carbon equivalent –calculated

98 using the expression previously given by other authors [6,25]- becomes 0.45%. The Cu
99 content detected is high enough to exert a slight corrosion inhibition effect [15].

100 The microstructure of cross-sectional views of the samples was observed in
101 metallographically prepared samples etched using Nital (5% HNO₃ in ethanol).
102 Microhardness Vickers HV0,1 (100 gf) profiles were carried out in the cross-sections of
103 the bars. Measurements started about 50 μm from the ribbed surface of the bar and
104 they were performed each 100 μm. For this study a Zwick Roell Indentec machine was
105 used.

106 For the electrochemical corrosion tests carried out in solution, two types of
107 samples were used: a) samples from the corrugated surface of the TMT bars, labelled
108 as “Ribbed surface”; and b) samples machined from TMT bars where the martensite
109 case had been fully removed, labelled as “Core”. The “Core” cylinders had a diameter
110 of 9 mm. Both types of samples were cut into 3-cm long cylinders, as can be seen in
111 **Figure 1**. The surface of the “Ribbed surface” samples were mechanically cleaned
112 before the test to erase the oxides formed due to the atmospheric exposure of the as-
113 received bars, using a Dremel Multipro tool. Before being immersed in the testing
114 solution, a copper wire was glued to one of the cross-sections of each sample using
115 silver paint. Then, both cross-sections were covered with epoxy coating to avoid their
116 interference in the measurement results.

117 The testing solution used to simulate that contained inside the pores of a
118 chloride contaminated concrete [16] was 0.1 M NaOH, 0.3 M KOH and 0.15 M NaCl.
119 The pH of this solution was 13.2. Each electrochemical measurement was repeated 4
120 times.

121 The galvanic current flowing between “Ribbed surface” and “Core” samples in
122 this solution was measured using a 263A Potentiostat/Galvanostat from PAR. For this
123 measurement, the ratio of the surfaces Ribbed surface/Core was 1.66.

124 Polarization curves and electrochemical impedance spectroscopy (EIS)
125 measurements were carried out for the “Ribbed surface” and “Core” samples in the
126 previously detailed solution. Moreover, these electrochemical tests were also
127 performed in short-circuited samples of “Core” and “Ribbed surface” connected through
128 a wire. This third type of samples will be called “Galvanic couple” hereafter.

129 A three-electrode cell was used in these studies. A saturated calomel electrode
130 (SCE) was used as reference electrode, and an AISI 316 stainless steel coiled wire as

131 counter electrode. The open circuit potential (OCP) of all the samples was allowed to
132 stabilize for 45 min in the testing solution. Then, the non-destructive EIS tests were
133 carried out and, finally, the polarization curves were performed. EIS measurements
134 were carried out from 100 kHz to 10 mHz applying a sinusoidal perturbation of 10
135 mV_{rms}. The polarization curves started at -200 mV from the previously determined
136 OCP, and the potential was increased towards more anodic values at a rate of 0.5
137 mV/s. Those electrochemical measurements were done using a Solartron Analytical
138 Potentiostat/Galvanostat from Ametek.

139 On the other hand, 50-cm long bars of the same TMT steel were used to
140 perform corrosion studies in concrete slabs with 500 x 265 x 100 mm dimensions. Six
141 slabs were manufactured, embedding in each one 10 steel bars with a 37-mm distance
142 between each bar. The cement used was CEM II/B-L 32.5 N, and the water/cement
143 ratio was 0.45. The aggregate/cement ratio was 5, with 1.5 being the ratio between
144 coarse aggregate and sand. A 3.3% CaCl₂ regarding the weight of cement was also
145 added to the mixture. The regions of the bars close to the concrete-air interface were
146 protected with an isolating tape, with an approximately 35-cm length of the bar exposed
147 to corrosion inside the concrete.

148 After casting, the 6 slabs were cured at high relative humidity and room
149 temperature for 28 days, and then the corrosion of the rebar was accelerated by
150 impressed currents. The current average density in each of the bars was approximately
151 30 $\mu\text{A}/\text{cm}^2$. This corrosion density was moderately higher than that determined for steel
152 in in-service structures exposed to chloride environments and high relative humidity
153 [26]. The method was already used and described in previous studies [27,28]. Bars
154 embedded in the different slabs were submitted to accelerated corrosion for different
155 times to achieve different levels of attack. After the accelerated corrosion tests in
156 concrete, the slabs were broken, and the oxides generated on the surface of the
157 reinforcing bars were cleaned using a HCl solution inhibited with urotrophine. The main
158 pits in each bar were identified and their morphology was characterized by
159 optoelectronic microscopy, with the measurements done using an Olympus DSX500.
160 Optoelectronic microscopy is a technique that has recently been used to characterize
161 the morphology of pits and evaluate its dangerousness in other materials [29].
162 Moreover, scanning electron microscopy (SEM) was used to check the relationship
163 between pit depth and microstructure.

164 **3. Results and discussion**

165 In **Figure 2**, optical microscopy images corresponding to etched cross-sections
166 of the TMT bars can be observed. In **Figure 2a**, the outer case -with a clearly darker
167 microstructure after the attack- can be easily distinguished from the inner region of the
168 corrugated bar. In **Figure 2b**, obtained at higher magnifications obtained, it can be
169 checked that the inner core of the bar is formed by ferrite and perlite, as corresponds to
170 a steel with a C content as that shown in **Table 1** and which has been cooled from the
171 austenitic state at a slow enough cooling rate. **Figure 2c** shows the transition region
172 between the core and the outer case. The thickness of the transition interlayer seems
173 to be much reduced, which suggests that the quenching procedure to form the outer
174 layer has been carried out adequately [6]. The presence of bainite in this interlayer has
175 been often mentioned in previous literature [10], but, for the studied bars, it is difficult to
176 assure with reliability the presence of this phase. Moreover, other authors have neither
177 found noticeable bainite in the microstructure of the bars nor have predicted its
178 presence by the modeling of the TMT process [8]. The microstructure observed in the
179 transition zone is compatible with ferritic and perlitic phases, which close to the
180 martensite case would become finer -with a smaller grain size- than in the bulk of the
181 bar (**Figure 2b**). In **Figure 2d**, the typical microstructure of martensite, has been
182 obtained by the quenching and tempering of the surface during bar manufacture, can
183 be observed.

184 Some representative microhardness profiles obtained measuring from the
185 surface of the bars towards regions where the micromechanical properties become
186 stable can be seen in **Figure 3**. These results show a plateau with the highest
187 hardness for regions close to the surface, proving the improvement in this property
188 caused by the formation of martensite (**Figure 2d**). The thickness of this high hardness
189 region depends on the exposure time to the water cooling during the martensite
190 formation and on the cooling-water flow rate [8]. The length of the highest hardness
191 plateau slightly oscillates (**Figure 3**). This result is coherent with the slight dispersion in
192 the thickness of the outer martensite case observed in different sections of the bars
193 and that can be guessed in images as that shown in **Figure 2a**. This lack of uniformity
194 for the outer case could be related to the dispersion in the prior austenite grain sizes in
195 the red heated steel during the bar processing [8]. Moreover, if the microhardness
196 profiles start from a rib of the surface, the highest hardness plateau is defined at
197 slightly higher values, probably because the faster cooling rate of this particular region
198 causes the formation of a finer grain martensite. The decrease in hardness after the
199 plateau is very steep, which corresponds to the observations in **Figure 2c**.

200 There is also another plateau for the lowest measured hardness (**Figure 3**).
201 The microhardness values can be considered completely stable from a surface
202 distance higher than about 2.2 mm, if the profiles start from a point between ribs.
203 Obviously, this stabilization distance is much higher if the measurement starts in a rib.
204 Between this plateau of complete stabilization and the decrease in hardness
205 corresponding to the transition zone, a region of hardness very slightly higher than that
206 of the plateau can be observed. This region with slightly higher hardness can be
207 identified with finer perlite and ferrite than in the bulk material observed close to the
208 martensite (**Figure 2**).

209 In chloride-containing solutions that, because of their pH, simulate those
210 contained inside the concrete pores, there is a galvanic current density flowing
211 between samples from the “Ribbed surface” and from the “Core” of the bars -as those
212 shown in **Figure 1**- when they are short-circuited. The sign of the measured current
213 always shows that the martensite from the surface of the ribbed bars acts as anode
214 against the material in the core. Time records with oscillations and small transitories, as
215 those shown in **Figure 4**, can be seen in this kind of experiments. To calculate the
216 galvanic current density (i_{galv}), the surface of the anodic samples -that is to say, the
217 area of the “Ribbed surface” samples- has been used. The mean values of i_{galv}
218 determined in the different experiments performed always ranged between 0.7 and 1.0
219 $\mu A/cm^2$. These results are coherent with the preferential corrosion of the martensite
220 case of TMT rebars in chloride contaminated concrete reported in other works [27,28].

221 Examples of the polarization curves obtained for “Ribbed surface” and “Core”
222 samples can be seen in **Figure 5**. Moreover, an example of one of the curves obtained
223 for “Galvanic couple” samples has also been included in the figure. All the curves are
224 quite similar, and they can be considered typical for systems that corrode actively at
225 moderate rates. In **Figure 6**, the most relevant data that can be calculated from curves,
226 as those shown in **Figure 5**, are plotted.

227 In **Figure 6a**, it can be seen that the corrosion potential (E_{corr}) determined for
228 the different types of samples are typical of active steel following the criterion proposed
229 by the ASTM C876 standard. There is some dispersion for measured E_{corr} values for
230 the same type of samples. Bearing in mind the overlapping of the error bars, it could be
231 concluded that the E_{corr} of the three studied types of samples are similar from a
232 statistical point of view. However, the highest average value observed for the “Galvanic
233 couple” can correspond to an increase in the cathodic area in these systems, which

234 slightly shifts the cathodic process to higher potentials, and so, increases the E_{corr} ,
235 which is the equilibrium potential between the anodic and the cathodic semireactions.

236 The corrosion current densities (i_{corr}) are also very similar for the three types of
237 samples (**Figure 6a**). All the measured i_{corr} are about one order of magnitude higher 0.1
238 $\mu\text{A}/\text{cm}^2$, which is usually assumed to be the limit value for corrosion of carbon steel
239 reinforcements [30]. The average value for the “Ribbed surface” is higher than for the
240 “Core” (**Figure 6a**). The i_{corr} for the “Galvanic couple” is calculated using the surface of
241 the martensite, instead of the surface of both short-circuited samples, the average i_{corr}
242 value increases up to a value similar to that of the “Ribbed surface”.

243 The most relevant information that can be drawn from the obtained polarization
244 curves are the Tafel slopes. In **Figure 6b**, it can be seen that, for the three systems, the
245 anodic Tafel slopes (b_a) are always higher than the cathodic Tafel slopes (b_c). This fact
246 means that the anodic process is the most hindered, and the i_{corr} is more controlled by
247 anodic semireaction than by the cathodic one. At any rate, as the difference between
248 b_a and b_c is not huge, a mixed control of the corrosion rate must be assumed, with a
249 lower influence of the cathodic process. The b_c values are quite similar for all the
250 studied systems, which implies that the oxygen reduction, that is the cathodic process
251 in this medium, is not clearly easier on the microstructure of one surface than in that
252 corresponding to the other. However, b_a is clearly higher for the “Core” than for other
253 samples. This indicates that the anodic process is less favored in the ferrite and perlite
254 than in the martensite. The b_a values allow to explain the i_{galv} observed and the
255 preferential corrosion of the martensite.

256 Hence, a galvanic couple is formed between martensite and ferrite, but its
257 performance does not coincide with that of the most well-known galvanic couples. The
258 anodic process is mainly located in the martensite, being able then to assume a certain
259 cathodic protection of the ferrite-perlite phases when the pits go deep down to the core
260 region of the bar. For this reason, it is necessary to use only the surface of the
261 martensite in the “Galvanic couple” samples to obtain reliable corrosion rates for the
262 electrochemical tests.

263 On the other hand, the ferrite-perlite phase does not have an E_{corr} that is
264 different from that of the martensite in the studied medium, and usually the cathodic
265 metal in typical galvanic couples has an E_{corr} which is clearly higher than the anodic
266 one. Moreover, the cathodic reaction of oxygen reduction is not more favored on the
267 surface of the cathodic metal than on the anodic, which would be another typical
268 characteristic of the most well-known galvanic couples. Due to the steep anodic branch

269 observed in the polarization curve for the “Ribbed samples” (**Figure 5**) and the small
270 increase in the E_{corr} that takes place due to formation of Galvanic couple, the
271 foreseeable increase in the i_{corr} for the “Galvanic couple” is lower than the experimental
272 dispersion determined for this parameter for the corroding systems studied. Thus,
273 short-circuiting ferrite-perlite with martensite would not meaningfully increase the
274 corrosion rate of the martensite in spite of the formed galvanic couple. In addition, it
275 should be borne in mind that, when the short circuiting takes place between the
276 material of the core and that of the case because of a pit, the ratio anodic area/cathodic
277 area is high, so the ability of the ferrite-perlite phase to increase the corrosion rate of
278 the martensite will become quite reduced.

279 Examples of the EIS spectra obtained for the “Ribbed surface”, “Core” and
280 “Galvanic couple” samples are shown, as Bode diagrams, in **Figure 7**. To obtain an
281 adequate simulation of spectra like these, a circuit equivalent as that proposed in
282 **Figure 8** has been necessary. In this circuit, R_{sol} is the solution resistance between the
283 counter electrode and the working electrode, and its influence can be seen at the
284 highest frequencies. The electric behavior of the passive layer is simulated by the
285 resistance R_{pas} and the constant phase element CPE_{pas} . Identification of the influence
286 of the passive layer with the time constant that appears in the spectra at medium-high
287 frequencies is commonly found in previous literature [31,32]. The corrosion activity
288 inside the pits is identified with the resistance R_{pit} and the capacitive behavior of CPE_{pit} ,
289 which appear in the spectra at lower frequencies. Moreover, to obtain a good
290 simulation of the experimental data at the lowest frequencies, it is necessary to include
291 a Warburg element related to the diffusion impedance through a finite thickness (W_s).
292 The equivalent circuit used to simulate the results is similar to the one already used to
293 simulate the electrochemical behavior of corroding steel in concrete [31,33].

294 In steel embedded in chloride contaminated concrete, a diffusion impedance
295 through a semi-infinite thickness is often identified at low frequencies. It has been
296 assumed that this impedance reflects the influence that the diffusion impedance of
297 oxygen through the concrete cover can have on the corrosion process. In solution tests
298 such as those performed in this study, the access of oxygen to the rebar surface is
299 higher and this hypothesis could be discarded, at least at moderate i_{corr} (**Figure 6a**).
300 The diffusion of ions through the oxide layer has also been previously proposed as
301 being responsible for the presence of diffusion impedance at the lowest-frequency part
302 of the spectra in simulated pore solutions [34] and in concrete [32]. Hence, the W_s
303 impedance could correspond to the diffusion through surface oxides. The polarization
304 results (**Figure 5**) are coherent with this hypothesis because of the region defined at

305 anodic overvoltages and high current densities where the i hardly increases its values
306 when E increases.

307 Due to their higher order of magnitude, the parameters that have the most
308 determining effect on the corrosion rate are R_{pit} and $W_s\text{-}R$, which have been
309 highlighted in bold in **Table 2**. For all the studied systems, R_{pit} is higher than $W_s\text{-}R$, so
310 the charge transfer resistance inside the pits can be identified as the rate determining
311 step. However, the difference between R_{pit} and $W_s\text{-}R$ is so small that it would be a
312 sizeable mistake to omit the influence of the ions diffusion through the oxide. The
313 global impedance of the process at low-frequencies (essentially $R_{\text{pit}}+W_s\text{-}R$) shows
314 values for “Ribbed surface” that are half of those obtained for the “Core”, matching the
315 trend obtained for the i_{cor} . (**Figure 6a**).

316 The influence of the microstructure on the development of the pits has been
317 checked carrying out accelerated tests in concrete. The SEM images in **Figure 9** allow
318 to verify that the pits tend to initially develop through the martensite, forming a slightly
319 jagged surface on this phase due to the attack (**Figure 9a**). When the corrosion
320 reaches the thin interlayer formed between the martensite and the ferritic and perlitic
321 region, the deepening of the attack seems restrained and the bottom of the pit
322 becomes smother (**Figure 9b**).

323 To perform a more exhaustive study regarding the pit morphology of TMT bars
324 in chloride contaminated concrete, the depth and surface area of the main pits detected
325 in corroded reinforcing TMT steel have been measured using optoelectronic
326 microscopy. Images such as that shown in **Figure 10** are obtained for the main pits
327 formed in the bars. The mass loss of each studied pit plotted in **Figures 11** and **12** has
328 been calculated from the volume of the pit given by its optoelectronic characterization
329 and using the density of the steel. Numerous pits whose mass losses differ more than
330 two orders of magnitude –in grams- have been considered for this study.

331 In **Figure 11**, it can be seen that the increase in volume of the pits is clearly
332 associated to an increase in the area of the pits mouths. Pits whose areas vary more
333 than two orders of magnitude –in mm^2 - have been detected. The pits associated to the
334 highest mass losses and with the highest mouth areas appear in bars embedded in the
335 slabs that have been corroded for the longest times.

336 At any rate, the results in **Figure 12** prove that the pits associated to the lowest
337 mass losses tend to have maximum depths lower than that of the martensitic case,
338 confirming the observation carried out for images like that in **Figure 9a**.

339 The obtained results suggest that the attack initially takes place in the
340 martensitic case and that, when the corrosion reaches the martensite-ferrite interlayer,
341 the pits tend to continue their growth by mouth widening through the martensitic case.
342 Only when the pits become very big and/or concrete cracking takes place, can this
343 trend disappear.

344 In **Figure 12**, the relationship between the volume/mass loss of each
345 characterized pit and its maximum depth is plotted. The pit depth is a parameter that,
346 for the pits most easily detectable by visual inspection, varies slightly. All the obtained
347 values from the pit depth differ in less than one order of magnitude, though the volume
348 of the pits is quite different. Moreover, most of the determined maximum pit depths are
349 between 1-2 mm. If it is borne in mind that the software always takes into account the
350 maximum height appearing in the image as a reference for calculating the height of the
351 pits, and that the height of ribs and nerves often influence this value, it is obvious that
352 the calculated maximum pit depth matches the thickness where the typical
353 microstructure of the core appears (**Figure 2**) and the lowest hardness plateau onsets
354 (**Figure 3**). Thus, these data confirm observations as those in **Figure 9b**, which
355 suggest that the attack tends to be stopped in the transition interlayer. The fact that
356 sometimes values for the pit depth slightly higher than the typical values obtained for
357 the martensitic case of the studied TMT steel have been obtained with this technique
358 could suggest that for the biggest pits, the cathodic protection that the martensite offers
359 to the ferrite and perlite would disappear in a moderately resistive medium such as
360 concrete or that the progress of the pits would be affected by the concrete cracking and
361 direct exposure to the atmosphere of part of the reinforcing steel.

362 **4. Conclusions**

363 The results obtained in this study reveal how the microstructure characteristic of
364 TMT affects the development of the pits in concrete with chlorides or another media
365 simulating it. The main conclusions that can be drawn the results obtained are:

- 366 • The i_{corr} of the martensite is slightly higher than that of the ferrite-perlite in
367 solution tests and their E_{corr} are similar.

- 368 • The galvanic coupling between the martensite and the ferrite-perlite in solution
369 tests proves that the martensite tends to act as anode and the ferrite-perlite as
370 cathode.
- 371 • The anodic semireaction of the martensite is more hindered than the cathodic
372 one in the testing solution, so a small increase in the cathodic surface that a pit
373 reaching to the core would imply, does not cause a meaningful increase in the
374 corrosion rate of the outer case.
- 375 • Results obtained in concrete proved that the depth of the attack is determined
376 by the microstructure of the TMT bars. Once the corrosion has reached the
377 ferritic-perlitic core, the attack tends to progress mainly by pit widening until the
378 volume of the pit is very large and/or the concrete covers cracks.

379 **Acknowledgments**

380 The authors acknowledge the financial support of Interreg SUDOE, through KrEaTive
381 Habitat project (Ref. SOE1/P1/E0307),

382

- [1] R. Felicetti, P. G. Gambarova, A. Meda. Residual behaviour of steel rebars and R/C sections after fire. *Constr. Build. Mater.* 23 (2009) 35-46. <https://doi.org/10.1016/j.conbuildmat.2009.06050>
- [2] A.Y. Elghazouli, K.A. Cashell, B.A. Izzuddin. Experimental evaluation of mechanical properties of steel reinforcement at elevated temperature. *Fire Saf. J.* 44 (2009) 909-919. <https://doi.org/10.1016/j.firesaf.2009.05.004>
- [3] M.A. Islam. Corrosion behaviour of high strength TMT steel bars for reinforcing cement concrete structures. *Proc. Eng.* 125 (2015) 623-630. <https://doi.org/10.1016/j.proeng.2015.11.084>.
- [4] S.K. Nandi, N.K. Tewary, J.K. Saha, S.K. Ghosh. Microstructure, mechanical properties and corrosion performance of a few TMT rebars. *Corr. Eng. Sci. Techn.* 51 (2016) 476-488. <https://doi.org/10.1080/1478422X.2016.11141744>.
- [5] S.K. Paul, P.K. Rana, D. Das, S. Chadra, S. Kundu. High and low cycle fatigue performance comparison between micro alloyed and TMT rebar. *Constr. Build. Mater.* 54 (2014) 170-179. <https://doi.org/10.1016/j.conbuildmat.2013.12.061>
- [6] I.R. Kabir, M.A. Islam. Hardened case properties and tensile behaviors of TMT steel bars. *Am. J. Mech. Eng.* 2 (2014) 8-4. <https://doi.org/10.12691/ajme-2-1-2>
- [7] H. Khalifa, G.M. Megahed, R.M. Hamouda, M.A. Taha. Experimental investigation and simulation of structure and tensile properties of Tempcore treated rebar. *J. Mater. Process. Techn.* 230 (2016) 244-253. <https://doi.org/10.1016/j.jmatprotec.2015.11.023>
- [8] K. Bandyopadhyay, J. Lee, J.-H. Shim, B. Hwang, M.-G. Lee. Modeling and experiment on microstructure evolutions and mechanical properties in grade 600 MPa reinforcing steel rebar subjected to TempCore process. *Mater. Sci. Eng. A* 745 (2019) 39-52. <https://doi.org/10.1016/j.msea.2018.12.079>
- [9] M. Mukherjee, C. Dutta, A. Haldar. Prediction of hardness of the tempered martensitic rim of TMT rebars. *Mater. Sci. Eng. A* 543 (2012) 35-43. <https://doi.org/10.1016/j.msea.2012.02.041>
- [10] A. Ghosh, M. Ghosh. Tensile and impact behavior of thermomechanically treated and micro-alloyed medium carbon steel bar. *Constr. Build. Mater.* 192 (2018) 657-670. <https://doi.org/10.1016/j.conbuildmat.2018.10098>.
- [11] F. Tariq, P. Bhargava. Residual mechanical behavior of (SD 500) hot rolled TMT reinforcing steel bars after elevated temperatures. *Constr. Build. Mater.* 190 (2018) 551-559. <https://doi.org/10.1016/j.conbuildmat.2018.09.008>
- [12] B. Das, A. Bakkar, N. Khutia, D. Das. Low cycle fatigue performance evaluation of TMT rebar. *Mater. Today: Proc.* 4 (2A) (2017) 2554-2563. <https://doi.org/10.1016/j.matpr.2017.02.109>
- [13] J.A. Gonzalez, E. Otero, S. Feliu, A. Bautista, E. Ramírez, P. Rodríguez, W. López. Some considerations on the effect of chloride ions on the corrosion of steel reinforcements embedded in concrete structures. *Mag. Concrete Res.* 50 (1998) 189-199. <https://doi.org/10.1680/mac.1998.50.3.189>
- [14] M. Otieno, J. Ikotun, Y. Ballin. Experimental investigations on the influence of cover depth and concrete quality on time to cover cracking due to carbonation-induced corrosion of steel in RC structures in an urban, inland environment. *Constr. Build. Mater.* 198 (2019) 172-181. <https://doi.org/10.1016/j.conbuildmat.2018.11.215>
- [15] B.K. Panigrahi, S. Srikanth, G. Sahoo. Effect of alloying elements on tensile properties, microstructure, and corrosion resistance of reinforcing bar steel. *JMEPEG* 18 (8) (2009) 1102-1108. <https://doi.org/10.1007/s11665-008-9336-z>
- [16] H. Tobarti-Sarraf, A. Poursaee. Corrosion of coupled steels with different microstructures in concrete environment. *Constr. Build. Mater.* 167 (2018) 680-687. <https://doi.org/10.1016/j.conbuildmat.2018.02.083>.

- [17] W. Zhu, R. François, C.S. Poon, J.-G. Dai. Influences of corrosion degree and corrosion morphology on the ductility of steel reinforcement. *Constr. Build. Mater.* 148 (2017) 297-306. <https://doi.org/10.1016/j.conbuildmat.2017.05.079>
- [18] C.A. Apostopoulos, S. Demis, V.G. Papadakis. Chloride-induced corrosion of steel reinforcement- Mechanical performance and pit depth analysis. *Constr. Build. Mater.* 38 (2013) 139-146. <https://doi.org/10.1016/j.conbuildmat.2012.07.087>
- [19] A. Castel, R. François, G. Arliguie. Mechanical behaviour of corroded reinforced concrete beams – Part 2: Bond and notch effects. *Mater. Struct.* 33 (2000) 545-551. <https://doi.org/10.1007/BF02480534>
- [20] Y. Ma, W. Qianj, Z. Guo, G. Wang, L. Wang, J. Zhang. Static and fatigue behaviour investigation of artificial notched steel reinforcement. *Materials* 10 (2017) 532. <https://doi.org/10.3390/ma10050532>
- [21] I. Fernández, J.M. Bairán, A.R. Martí. Corrosion effects on the mechanical properties of reinforcing steel bars. Fatigue and σ - ϵ behaviour. *Constr. Build. Mater.* 101 (2015) 772-783. <https://doi.org/10.1006/j.conbuildmat.2015.10.139>
- [22] E.C. Paredes, A. Bautista, S.M. Alvarez, F. Velasco. Influence of the forming process of corrugated stainless steel on their corrosion behaviour in simulated pore solutions. *Corros. Sci.* 58 (2012) 52-61. <https://doi.org/10.1016/j.corsci.2012.01.010>
- [23] W. Zhu, R. François. Y. Liu. Propagation of corrosion and corrosion patterns of bars embedded in RC beams stored in chloride environment for various periods. *Constr. Build. Mater.* 145 (2017) 147-156. <https://doi.org/10.1016/j.conbuildmat.2017.03.210>
- [24] Z. Zhao, L. Fu. The probability distribution of pitting for accelerated corrosion reinforcement. *Case Studies Contr. Mater.* (*in press*). <https://doi.org/10.1016/cscm.2018.e00193>
- [25] R. Datta, R. Veeraraghavan, K.L. Rohira. Weldability characteristics of torr and corrosion-resistant TMT bars using SMAW process. *Mater. Eng. Perform.* 11 (2002) 369-375. <https://doi.org/10.1361/105994902770343881>
- [26] C. Andrade. C. Alonso. On site measurements of corrosion rate of reinforcements. *Constr. Build. Mater.* 15 (2001) 141-145.
- [27] E. Moreno, A. Cobo, G. Palomo, M.N. González. Mathematical models to predict the mechanical behaviour of reinforcements depending on their degree of corrosion and the diameter of the rebars. *Constr. Build. Mater.* 61 (2014) 156-163. <https://doi.org/10.1016/j.conbuildmat.2014.03.003>
- [28] A.M. Bazán, A. Cobo, J. Montero. Study of mechanical properties of corroded steels embedded in concrete with the modified surface length. *Constr. Build. Mater.* 117 (2016) 80-87. <https://doi.org/10.1017/jconbuildmat.2016.04.109>
- [29] G. Monrrabal, A. Bautista, S. Guzman, C. Gutierrez, F. Velasco. Influence of the cold working induced martensite on the electrochemical behavior of AISI 304 stainless steel surfaces. *J. Mater. Res. Techn.* (*in press*). <https://doi.org/10.1016/j.jmrt.2018.10.004>
- [30] A. Pachón-Montaño, J. Sánchez-Montero, C. Andrade, J. Fullea, E. Moreno, V. Matres. Threshold concentration of chlorides in concrete for stainless steel reinforcement: Classic austenitic and new duplex stainless steel. *Constr. Build. Mater.* 186 (2018) 495-502. <https://doi.org/10.1016/j.conbuildmat.2018.07.081>
- [31] J. Shi, J. Ming, W. Sun, Y. Zhang. Corrosion performance of reinforcing steel in concrete under simultaneous flexural load and chlorides attack. *Constr. Build. Mater.* 149 (2017) 315-326. <https://doi.org/10.1016/j.conbuildmat.2017.05.092>
- [32] D.V. Ribeiro, J.C.C. Abrantes. Application of electrochemical impedance spectroscopy (EIS) to monitor the corrosion of reinforced concrete: A new approach. *Constr. Build. Mater.* 111 (2016) 98-104. <https://doi.org/10.1016/j.conbuildmat.2016.02.047>

- [33] A. Bautista, E.C. Paredes, S.M. Alvarez. F. Velasco. Welded, sand-blasted stainless steel corrugated bars in non-carbonated and carbonated mortars: A 9-year corrosion study. *Corros. Sci.* 102 (2016) 363-372. <https://doi.org/10.1016/j.corsci.2015.10.029>
- [34] S. Mundra, M. Criado, S.A. Bernal, J.L. Provis. Chloride-induced corrosion of steel rebars in simulated pore solutions of alkali-activated concretes. *Cement Concrete Res.* 100 (2017) 385-397. <https://doi.org/10.1016/j.cemconres.2017.08.006>

TABLES

Table 1. Chemical composition of the studied B-500-SD bars.

Chemical composition (%)								
C	Mn	S	Si	Cu	Ni	Mo	V	Fe
0.21	0.86	0.02	0.29	0.34	0.09	0.02	<0.001	Balance

Table 2. Results obtained from the simulation of the EIS spectra obtained in simulated pore solution.

	R_{sol} ($\Omega \cdot cm^2$)	R_{pas} ($\Omega \cdot cm^2$)	C_{pas} ($\mu F \cdot cm^2 \cdot s^{-n-1}$)	n_{pas}	R_{pit} ($k\Omega \cdot cm^2$)	C_{pit} ($\mu F \cdot cm^2 \cdot s^{-n-1}$)	n_{dl}	$Ws-R$ ($k\Omega \cdot cm^2$)	$Ws-T$ (s)	$Ws-P$
Ribbed surface	7.1±0.5	13±5	78±24	0.81±0.03	5±2	151±56	0.77±0.01	4±1	85±7	0.50±0.01
Core	6.7±0.4	13±1	32±5	0.89±0.04	13±5	48±5	0.87±0.03	7±1	9±5	0.43±0.03
Galvanic couple	7.6±0.5	14±2	7±2	0.80±0.01	11±1	100±5	0.78±0.01	7±2	19±4	0.50±0.01

Figure legends

Figure 1. Image of the samples used for the electrochemical studies in simulated pore solution.

Figure 2. Cross sectional images of the TMT reinforcing bar: a) whole cross-sectional view; b) microstructure of the core of the bar; c) microstructure of the transition region; d) microstructure of the outer region of the bar.

Figure 3. Microhardness profiles carried out on cross sections of the bars.

Figure 4. i_{galv} flowing between samples of corrugated surface of the bars and samples from the core of the bars when they are short-circuited and immersed in simulated pore solution.

Figure 5. Examples of polarization curves in simulated pore solution.

Figure 6. Results obtained from polarization curves as those shown in Figure 5: a) values corresponding to the i_{corr} and the E_{corr} of the studied samples; b) Tafel slopes calculated for the studied systems.

Figure 7. Examples of the EIS spectra obtained in simulated pore solution and plotted using Bode diagrams.

Figure 8. Equivalent circuit used to simulate the obtained EIS spectra.

Figure 9. Cross sectional views of pits generated in bars embedded in a chloride contaminated concrete slab. **a)** Pit with a moderate depth; **b)** Deep pit.

Figure 10. Example of the optoelectronic microscopy image for pit generated in a chloride contaminated concrete slab.

Figure 11. Relationship between the mass loss of each pit and its mouth surface. Results obtained from the optoelectronic characterization of the main pits formed on the six different studied chloride contaminated concrete slabs.

Figure 12. Relationship between the mass loss of each pit and its maximum depth. Results obtained from the optoelectronic characterization of the main pits formed on the six different studied chloride contaminated concrete slabs.

Figure 1

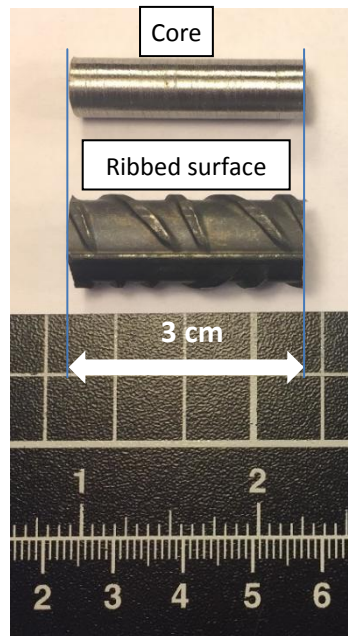


Figure 2

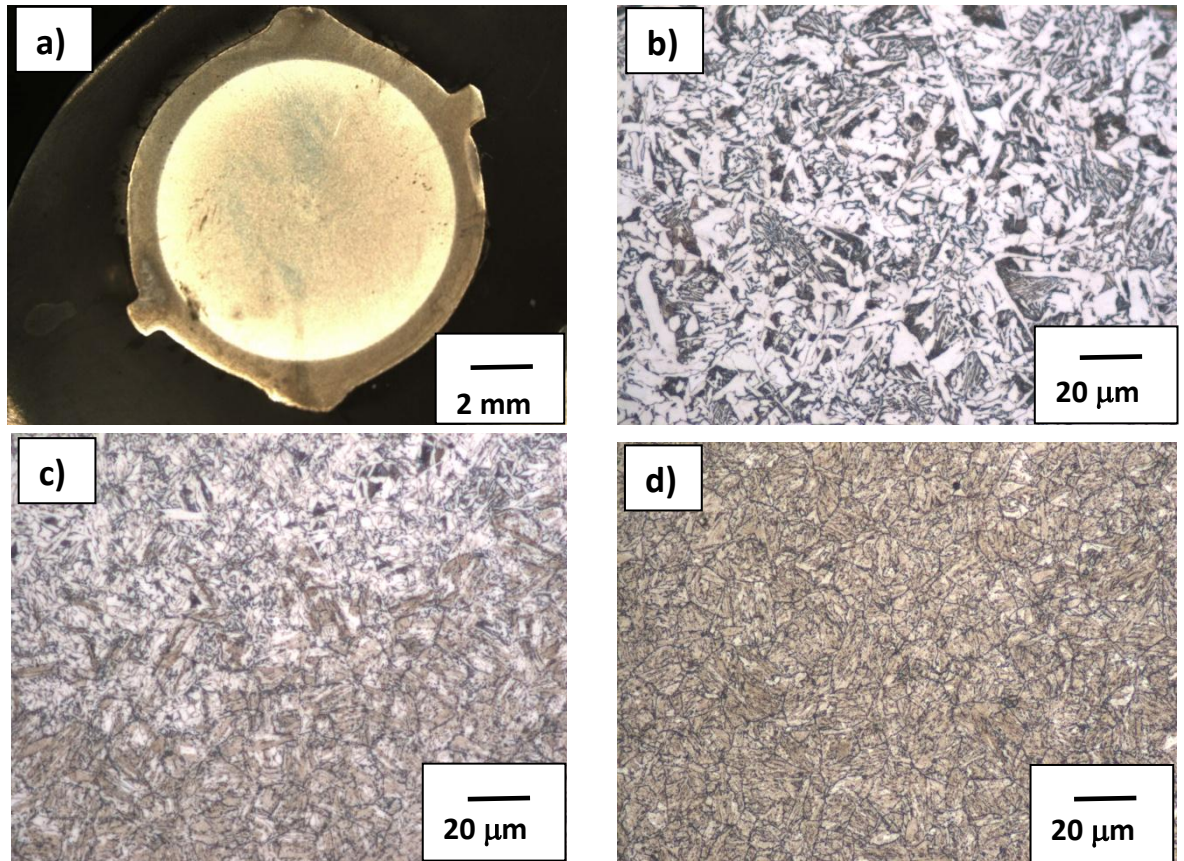


Figure 3

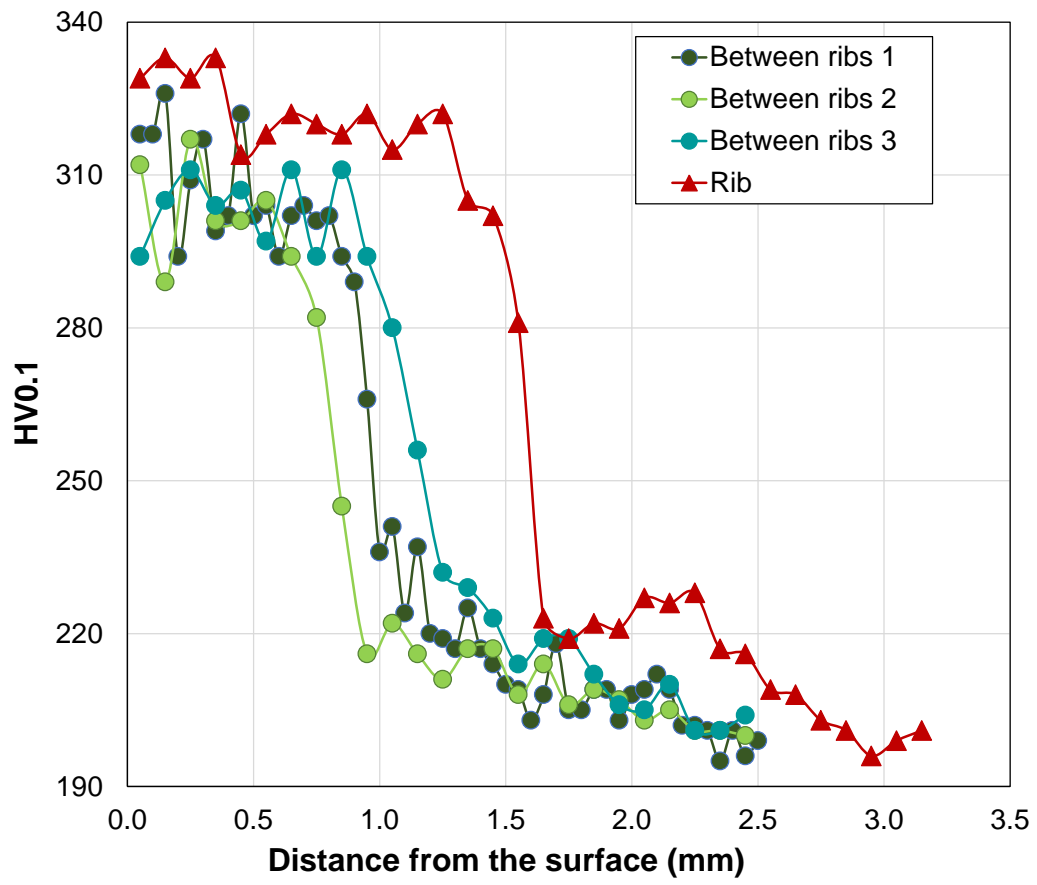


Figure 4

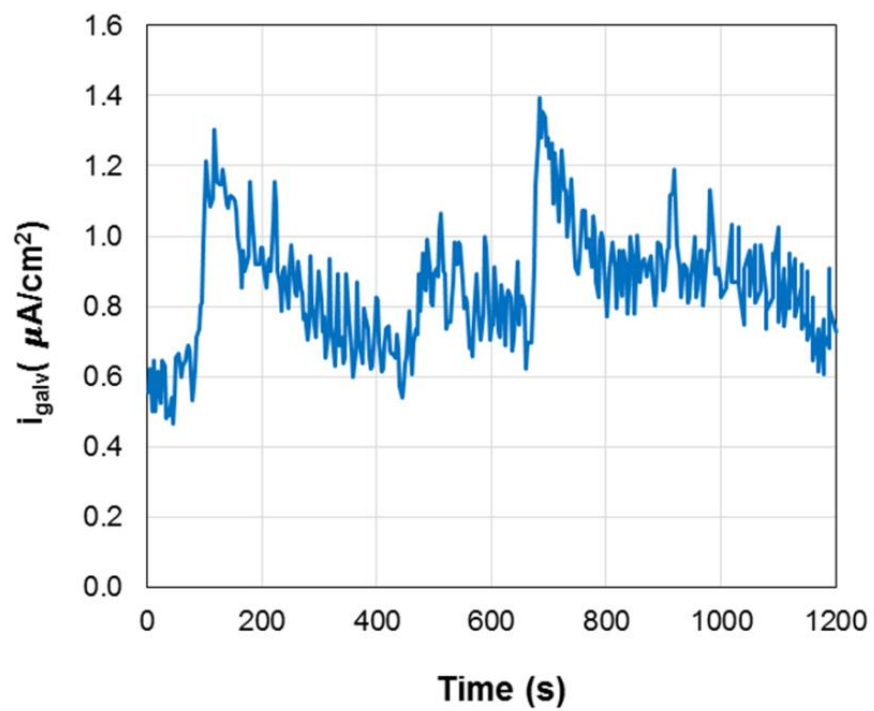


Figure 5

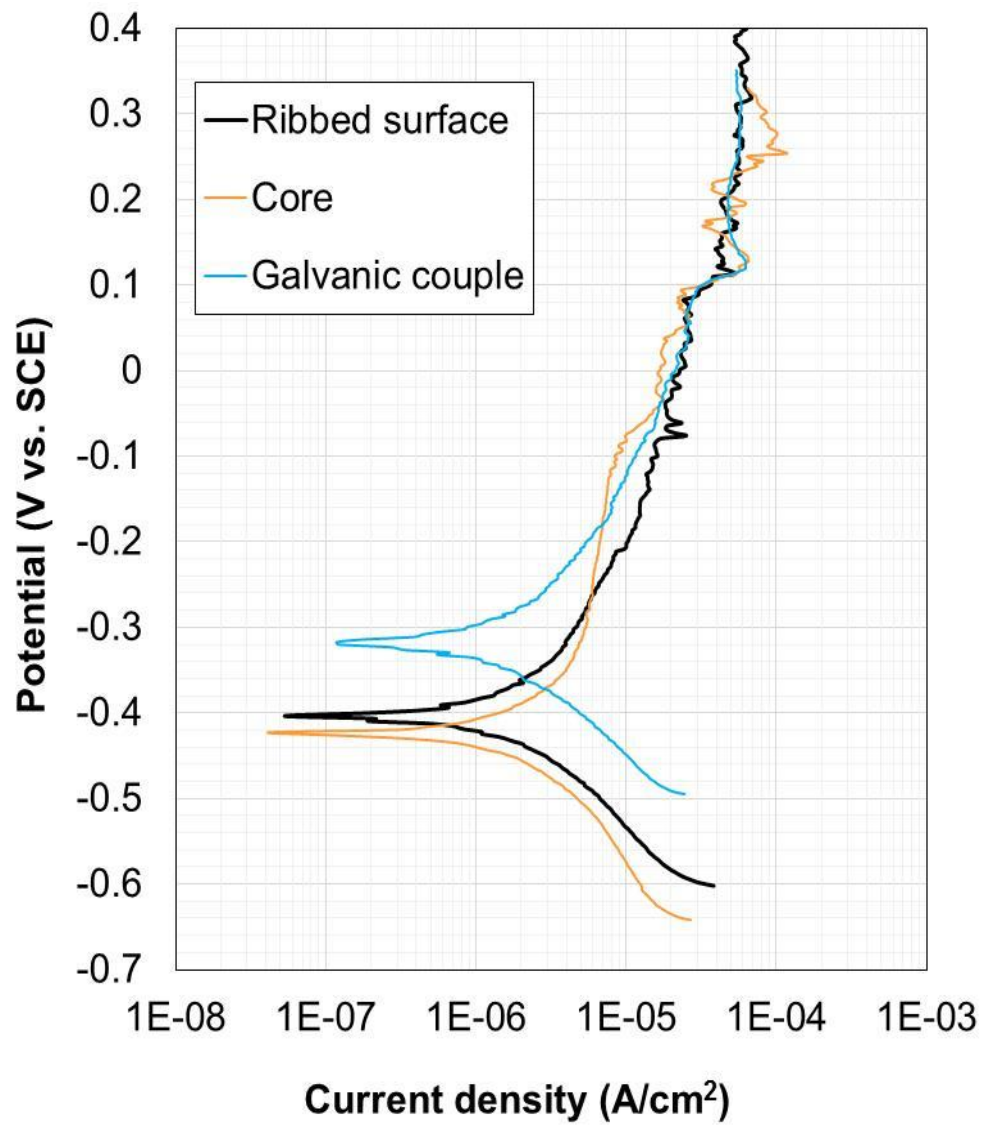


Figure 6

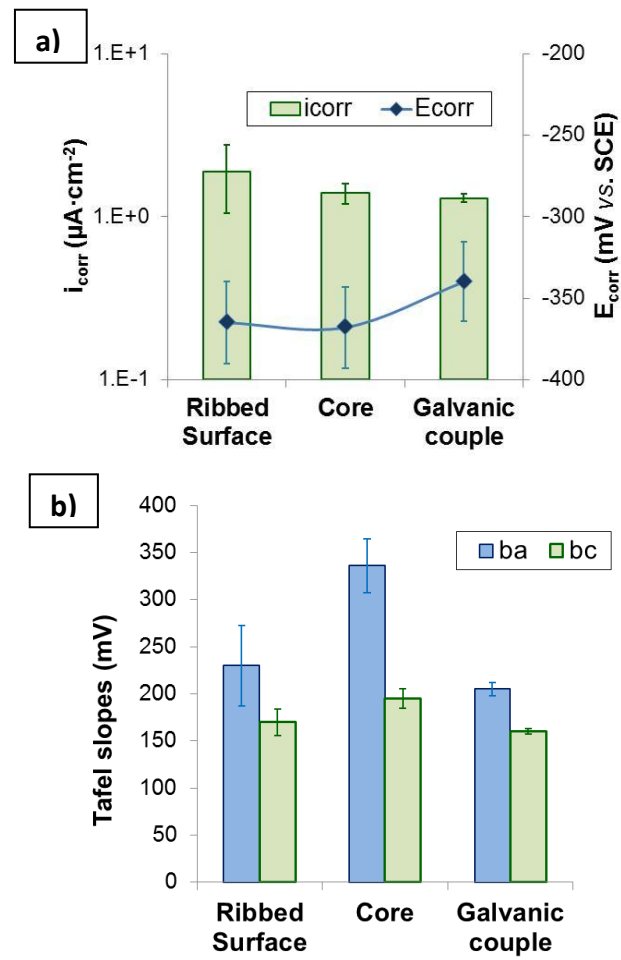


Figure 7

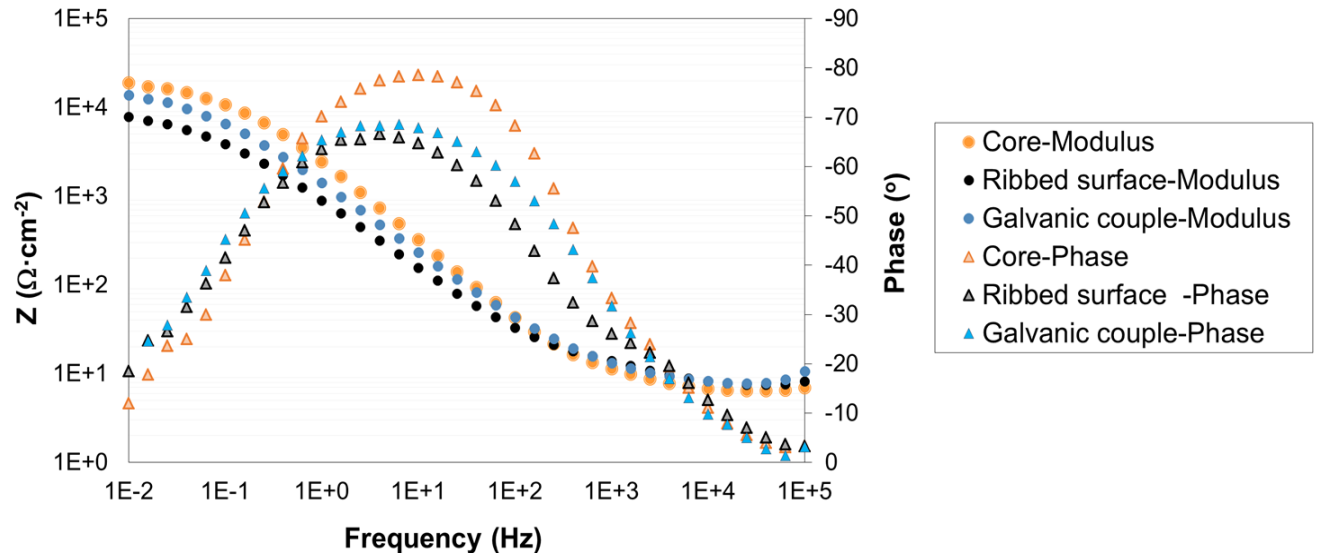


Figure 8

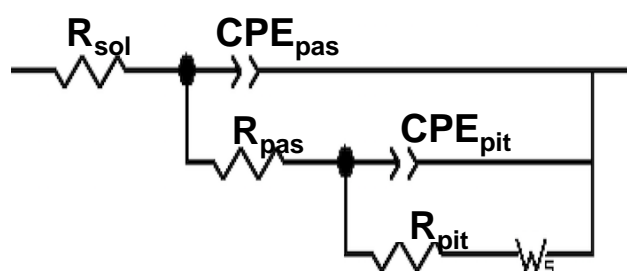


Figure 9

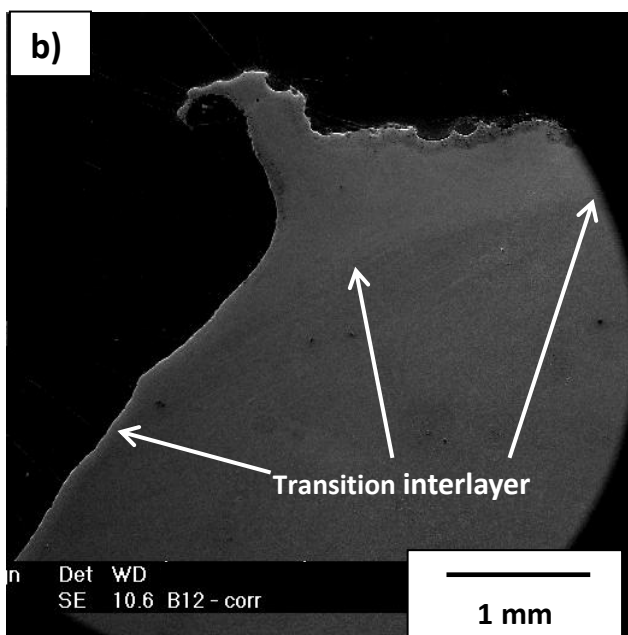
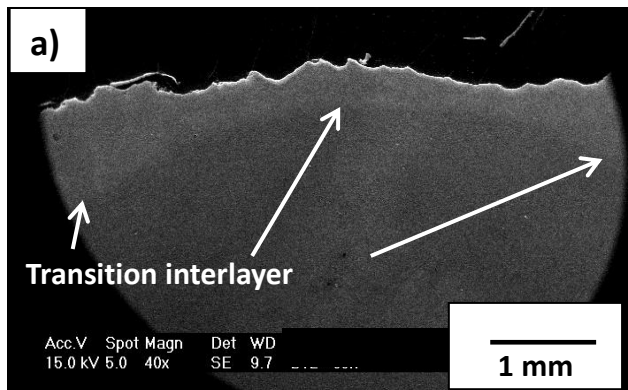


Figure 10

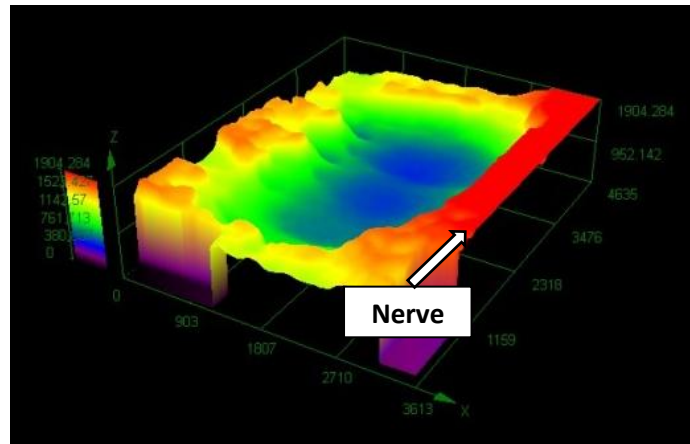


Figure 11

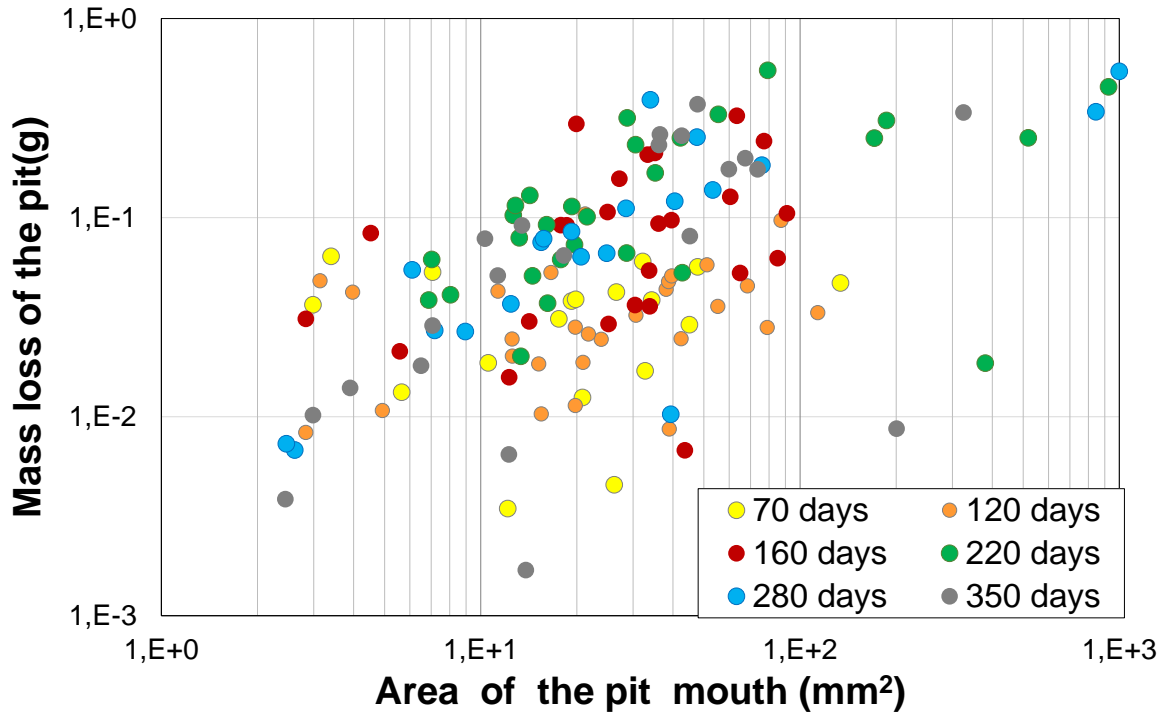
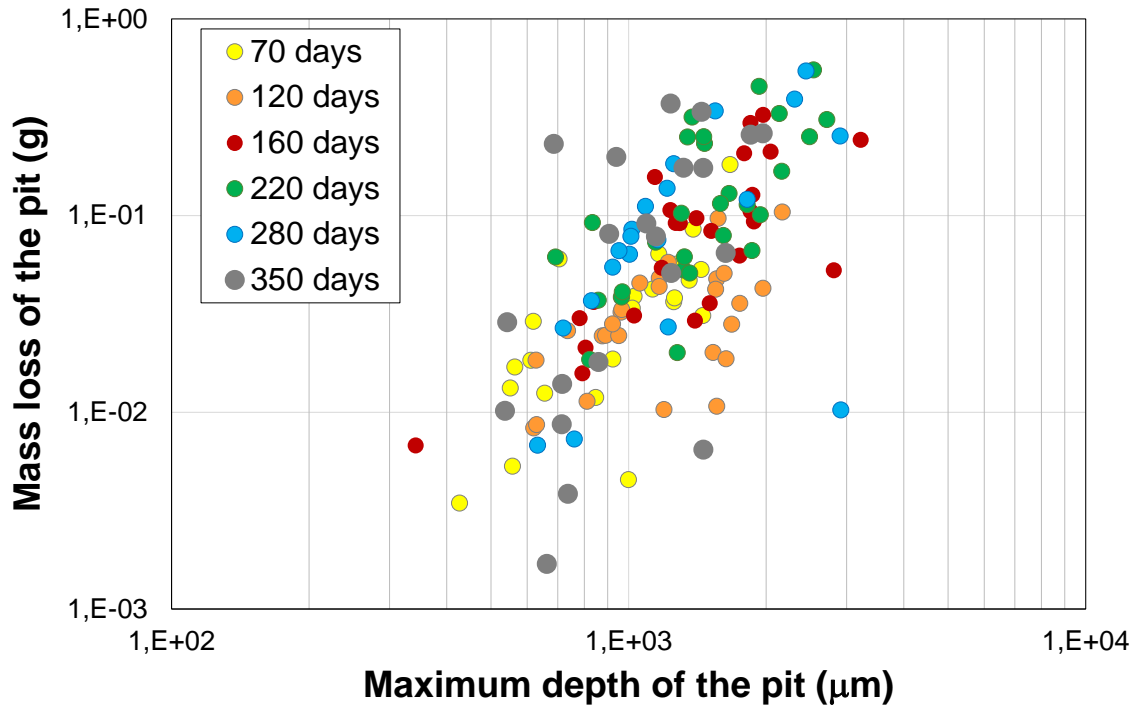


Figure 12



Highlights:

- Corrosion studies of TMT bars in simulated pore solutions and in concrete slabs.
- The outer martensite acts as anode and the core as cathode when both parts of the bar are coupled.
- The core material does not meaningfully increase the corrosion rate of the outer martensite.
- The usual depth of the pits is related to the microstructure of the TMT bars.
- When pits reach the martensite-core interlayer, they progress by mouth widening.

Graphical abstract

